



Armin Kögel · Nuri Aksel

Stability of the channel flow—new phenomena in an old problem

Received: 5 August 2019 / Revised: 16 October 2019 / Published online: 16 December 2019
© Springer-Verlag GmbH Austria, part of Springer Nature 2019

Abstract In this article, we show an unexpected effect of side walls on the stability of gravity-driven viscous film flows over flat substrates in an open channel. Until now, it was assumed that side walls have a stabilizing effect on the flow, but the qualitative structure of the neutral curve remains the same. We show a fragmentation of the stability chart that was only known from undulated substrates. The cause of the fragmentation is a distinct damping of waves with a certain frequency that is independent of the underlying instability of the two-dimensional flow. This paper provides a detailed parameter study that identifies the channel width as the decisive parameter for the damping frequency. In addition, the damping is not an effect of flat side walls exclusively, since corrugated side walls have qualitatively the same impact on the stability chart. Furthermore, we demonstrate that the curvature of the emerging wave's crest line has a non-monotonous dependency on the frequency and shows a distinct maximum. The frequency of this maximum shows the same behavior as the damping frequency when the channel width is varied. We therefore assume a relation between the wave's curvature and its growth rate, both massively affected by the side walls.

1 Introduction

Viscous thin film flows are present in a large number of industrial and natural systems. They appear among others in coating [1–3] and heat exchanging applications [4, 5]. In the environment, viscous films can be found in glaciers [6], avalanches [7] and debris flows [8] as well as in biofilms [9] and tear films [10]. It is of special interest to understand the stability phenomena of film flows and especially the means of modifying the stability against free surface perturbations.

The basic flow over a flat substrate of infinite extent is known as the Nusselt flow [11]. Since in real applications the flow is almost always restrained by side walls, Scholle and Aksel [12] studied the effect of the side walls analytically. The experimental work was done by Haas et al. [13]. There are two competing effects on the flow: first, the velocity of the fluid is slowed down in the vicinity of the side walls compared to the center of the channel due to the no-slip condition. Second, the capillary elevation at the side walls leads to a locally higher film thickness and thus to an increased fluid velocity. Depending on other system parameters, these two effects can result in a velocity overshoot in the vicinity of the side walls. Particularly for high film thicknesses, no overshoot is possible.

The instability of film flows was first experimentally studied by Kapitza [14], respectively Kapitza and Kapitza [15], who observed spontaneously appearing surface waves above a critical volume flux. The analytical studies of Benjamin [16] and Yih [17] showed a long-wave instability for the flow over a flat surface of infinite extent, tilted by an angle α , at the critical Reynolds number $Re_c = (5/4) \cot \alpha$.

A. Kögel (✉) · N. Aksel
Department of Applied Mechanics and Fluid Mechanics, University of Bayreuth, 95440 Bayreuth, Germany
E-mail: Armin.Koegel@uni-bayreuth.de

In natural and technical systems, the substrates are generally not perfectly flat, but corrugated. Therefore, a major task in the studies of film flows is to understand the effects of undulated substrates on the stability of the system. Analytical and experimental studies were carried out for weakly undulated substrates, and it was found that they have a slightly stabilizing effect [18,19]. For strongly undulated substrates, there are stabilizing as well as destabilizing effects [20]. An important fact is that undulated substrates do not only shift the neutral curve, but can change the entire shape of the linear stability chart. A fragmentation of the neutral curve and a formation of an unstable island were first described theoretically by Heining and Aksel [21]. Their prediction was experimentally confirmed by Pollak and Aksel [22], who reported on crucial flow stabilization and multiple instability branches in the linear stability chart of gravity-driven viscous films flowing down a wavy incline of sinusoidal shape. It is possible to switch between different types of stability isles by varying system parameters, e.g., the inclination angle, or the viscosity or the corrugation's periodicity [23]. The exact shape of the corrugation, however, has no considerable influence on the stability chart [24]. New findings show that there are only a few different patterns of stability islands. Schörner and Aksel [25] unveiled a universal pathway along which the stability charts evolve when the system parameters are changed. A detailed discussion of the effects of undulated substrates on the stability of film flows as well as the steady state flow can be found in the review of Aksel and Schörner [26].

The effect of side walls on the critical Reynolds number of film flows was experimentally studied by Vlachogiannis et al. [27]. They found a significant increase in Re_c for small channel widths. Also the surface tension was found to play a considerable role for the stability of channel flows [28]. A transition from long-wave to short-wave instability in the vicinity of the side walls was described by Pollak et al. [29]. The structure of the side walls has a major impact on the stability of the flow: Kögel and Aksel [30] found a massive stabilization caused by corrugated side walls depending on the streamwise length scale of the corrugation. For very short and very large length scales, the critical Reynolds number approximates the value of flat side walls, but at intermediate length scales there is a distinct maximum in the stabilization.

The influence of the side walls on the surface waves is not only visible in the stability of the flow, but also in the shape of the emerging waves. Leontidis et al. [31] observed a parabolic crest line which curvature depends on several system parameters, especially the channel width.

The aim of the present study is to show completely new phenomena in the stability of channel flows. Until now, it was assumed that flat side walls have a stabilizing effect on the flow, but the qualitative structure of the neutral curve remains the same. We show a fragmentation of the stability chart that was only known from undulated substrates. The cause of this fragmentation is a distinct damping of selected waves. In this paper, we show the relevant system parameters that affect this damping. To this end, we use different measurement techniques to gain information on the linear stability of the flow as well as the dispersion relation and the curvature of the generated waves. We present a detailed parameter study that shows the dependencies of the frequencies and the wavelengths of the damped waves on several system parameters, namely the Reynolds number, the channel width, the inclination angle and the viscosity. We investigate the dependency of the curvature on the frequency and channel width and show an interesting new phenomenon. Finally, we make a connection between the curvature of the wave's crest line and the damping phenomenon.

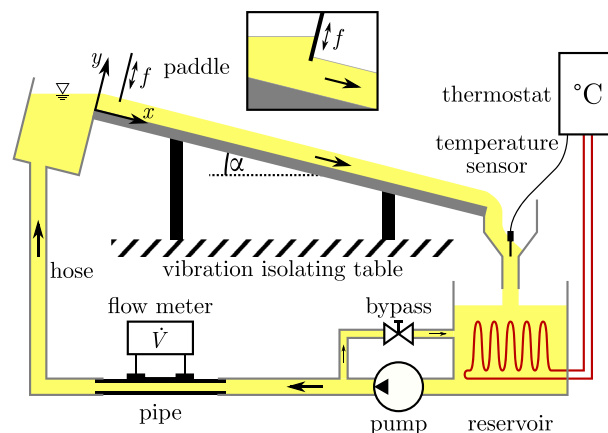


Fig. 1 Schematic plot of the experimental setup

2 Studied system and experimental setup

Our experimental setup is schematically shown in Fig. 1. The measurements were carried out in an open channel with a flat substrate of aluminum and flat side walls of Plexiglas. Two movable aluminum side walls can be placed within the channel to change the channel width B . The whole channel can be tilted by an angle α and is mounted on a vibration isolating table to reduce parasitic vibrations from the surrounding (mainly the pump and thermostat).

The fluid is pumped by an eccentric pump from the reservoir to the channel inlet through flexible hoses. A non-inversive flow meter type *Deltawave C* from *Systec controls* is mounted on a stiff PVC pipe. The adjustable bypass has multiple advantages for the system: first, pressure surges from the pump can partially escape through the bypass and therefore have a smaller impact on the fluid within the channel. Second, the volume flux \dot{V} can be adjusted more precisely, and third, it is possible to set the same volume flux with different pumping capacities. The last point is necessary to investigate measurement artifacts (e.g., parasitic frequencies) produced by the pump. At the inlet of the channel, there is an inflow tank to calm the fluid and allow a steady inflow into the channel. A paddle that is permanently dipped into the fluid surface (see the inlay of Fig. 1) is used to excite sinusoidal waves with adjustable frequency f and amplitude A that evolve downstream along the channel. The inflow tank and the paddle have the same width as the channel without the inner side walls, denoted as maximum channel width. The paddle is placed few centimeters in front of the taper of the channel caused by the inner side walls; please see, e.g., Fig. 3 for a three-dimensional view of the whole channel. Depending on the channel width and the volume flux, there are different inflow effects right after the taper, e.g., an acceleration of the surface velocity or a spanwise flow component. These effects decay after a certain distance and have to be considered when performing an experiment. At the end of the channel, the fluid flows back into the reservoir and passes a temperature sensor. A thermostat keeps the fluid at a fixed temperature T .

As fluid, we used two different mixtures of the silicone oils *Elbesil 50* and *Elbesil 200* with different viscosities, denoted as *Elbesil 140* and *Elbesil 100*. The density ρ , dynamic viscosity η , kinematic viscosity ν , surface tension σ and Kapitza number $Ka = \sigma/(\rho g^{1/3} \nu^{4/3})$ of each fluid, as well as the temperature at which the experiments were performed, are given in Table 1. Unless otherwise stated, the liquid *Elbesil 140* was used.

To eliminate measurement artifacts produced by the setup, we performed measurements in three different channels with different peripherals. The dimensions of the channels and the used silicone oil, pump, and thermostat are given in Table 2. All pumps are from *Johstadt*, and all thermostats are from *Haake*. All three setups have also different pipe systems, i.e., different diameters and lengths.

For our experiments, we use the definition of the Reynolds number

$$Re = \frac{3\dot{V}}{2\nu B}. \quad (1)$$

The finite width of our channel leads to a reduced flow velocity in the vicinity of the side walls [13,32]. For all channel widths, this effect is small enough to not affect the flow in the center of the channel. The difference between the local Reynolds number $Re_{\text{local}} = hu_{\text{surf}}/\nu$ (with the film thickness h and the surface velocity u_{surf}) and the Reynolds number defined in Eq. 1 is much smaller than the measurement accuracy. Particularly for large channel widths, this effect vanishes. The effect of the capillary elevation at the side walls and the

Table 1 Fluid properties

Notation	ρ (kg/m ³)	η (mPa s)	ν (mm ² /s)	σ (mN/m)	Ka	T (°C)
<i>Elbesil 140</i>	962.7 ± 0.4	136.7 ± 0.5	142.0 ± 0.5	20.25 ± 0.11	1.32 ± 0.01	24.0 ± 0.1
<i>Elbesil 100</i>	964.9 ± 0.4	99.4 ± 0.5	103.0 ± 0.5	20.14 ± 0.07	2.02 ± 0.01	23.0 ± 0.1

Table 2 Properties of the different setups

Channel number	Length (mm)	Maximum width (mm)	Silicone oil	Pump	Thermostat
1	2000	255	<i>Elbesil 140</i>	<i>AFJ 40.1B</i>	<i>TC300</i>
2	1400	170	<i>Elbesil 140</i>	<i>SK90L/4</i>	<i>N6</i>
3	2000	170	<i>Elbesil 100</i>	2× <i>AFJ 15.1B</i> (parallel)	<i>TC300</i>

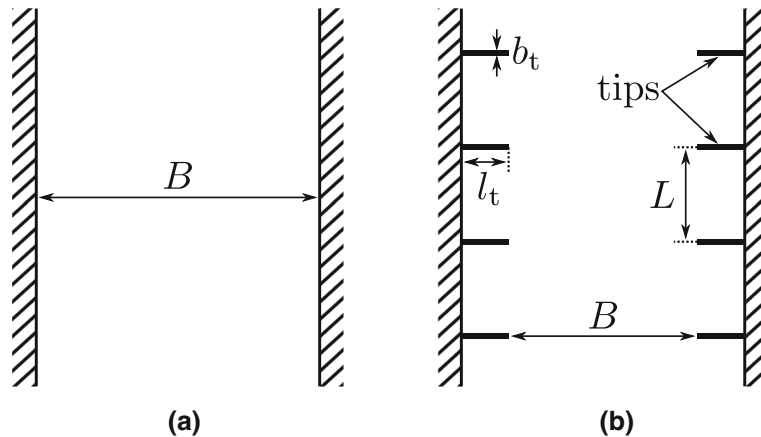


Fig. 2 Geometric dimensions of the channel (top view) for **a** flat and **b** corrugated side walls

influence of the surface tension can also be neglected, since our film thickness is sufficiently large [13,32] and the Kapitza number is sufficiently low [28].

We performed experiments at three inclination angles $\alpha = 5^\circ, 10^\circ$ and $15^\circ (\pm 0.1^\circ)$ and varied the channel width B from 84 up to 255 mm (± 0.5 mm). The excitation frequency f ranges from 1 to 15 Hz (± 0.01 Hz) and the Reynolds number Re from 5 to 60 (± 0.5).

For the sake of comparison, we performed additional experiments with corrugated side walls. Since a fragmentation of the neutral curve is only known for plane flows over corrugated substrates, we want to find out whether corrugated side walls have a similar effect on the stability of the flow. The geometric dimensions are shown in Fig. 2: for flat side walls the only geometric length is the channel width B . For corrugated side walls we attached tips with a length $l_t = 8$ mm and a width $b_t = 1$ mm symmetrically on both walls perpendicular to the bottom. The tips are just as high as the side walls and therefore much larger than the film thickness. The channel width B is defined as the distance between two opposing tips. The streamwise distance between two tips is denoted as L and was varied from 5 to 100 mm with an error of 0.1 mm.

3 Determination of the linear growth rate and wavelength in the two-dimensional case

To study the effect of a finite channel width, we want to compare the stability of the channel flow with the stability of the classical film flow without side walls (plane flow), both over flat substrates. Since in our experimental system side walls are inevitable, we use a two-dimensional theoretical model to describe the stability of the plane flow of infinite extent [16,17]. The calculation of the growth rate and the wavelength of waves with excitation frequency f follows in large parts the works of Yih [17,33]: they used a disturbance approach on the basic flow and derived the dimensionless Orr–Sommerfeld equation with corresponding boundary conditions:

$$0 \leq y^* \leq 1 : \quad \psi^{*''''} - 2k^{*2}\psi^{*''} + k^{*4}\psi^* = ik^*\text{Re}((U^* - c^*)(\psi^{*''} - k^{*2}\psi) - U^{*''}\psi^*), \quad (2)$$

$$y^* = 0 : \quad \psi^* = 0, \quad (3)$$

$$y^* = 0 : \quad \psi^{*'} = 0, \quad (4)$$

$$y^* = 1 : \quad \psi^{*''} = -(k^{*2} + \frac{2}{1 - c^*})\psi^*, \quad (5)$$

$$y^* = 1 : \quad \psi^{*'''} = (3k^{*2} + ik^*\text{Re}(1 - c^*))\psi^{*'} - \frac{ik^*}{1 - c^*} \left(\frac{2}{\tan \alpha} + k^{*2}\text{Ka} \left(\frac{2}{\text{Re}^2 \sin \alpha} \right)^{\frac{1}{3}} \right) \psi^*. \quad (6)$$

In this set of equations, all variables and parameters are dimensionless. The spatial coordinate perpendicular to the bottom is denoted as y^* . The bottom is at $y^* = 0$, the undisturbed surface at $y^* = 1$. The prime denotes a differentiation to y^* . The stream function of the disturbance is denoted as ψ^* , whereas k^* is the wave number and c^* the phase velocity of the wave. The inclination angle is denoted as α , the Reynolds number as Re , and the Kapitza number as Ka . The undisturbed basic flow is

$$U^* = 2y^* - y^{*2}. \quad (7)$$

In this model which is common in the literature a *temporal instability* is assumed; therefore, the wave number k^* is real and the phase velocity c^* is complex. In this case, a wave with given wave number grows/decays in time, not in space. Since in our experimental setup we measure the *spatial instability* where we control the frequency f^* (more precisely, the dimensional frequency f) of the wave and not the wave number k^* , the wave grows/decays in space. To introduce the frequency f^* in the set of equations, we have to rewrite the phase velocity:

$$c^* = \frac{2\pi f^*}{k^*}. \quad (8)$$

To calculate the spatial instability, we set the frequency f^* real and the wave number k^* complex. We have to solve the new set of equations to obtain its eigenvalue k^* . To this aim, we use a numerical shooting method. From the complex wave number k^* , we can now derive the wavelength

$$\lambda^* = \frac{2\pi}{\Re(k^*)} \quad (9)$$

and the spatial growth rate

$$b^* = -\Im(k^*) \quad (10)$$

of the wave with frequency f^* . The neutral curve $b^* = 0$ can be derived by varying \Re at a fixed f^* and finding the root of b^* using Newton's method.

4 Measurement methods

4.1 Measurement of the linear instability

To measure the linear instability of our system, a similar setup as in previous works was used [22–24, 29, 34–37]. Figure 3 gives a three-dimensional view of the channel. Within the symmetry plane of the channel, two parallel laser beams were reflected at the fluid surface and projected onto the screen. A sinusoidal wave with frequency f causes an oscillation of the spots with the same frequency:

$$A_1(t) = A_1^0 \sin(2\pi f t - \varphi_1), \quad A_2(t) = A_2^0 \sin(2\pi f t - \varphi_2). \quad (11)$$

A_1^0 and A_2^0 denote the amplitudes of the signals, whereas φ_1 and φ_2 denote arbitrary phases at $t = 0$. In short, the amplitudes of the signals A_1^0 and A_2^0 were proportional to the oscillation of the surface slope and therefore to the amplitudes of the wave at the corresponding reflection spots. Please see, e.g., the work of Pollak et al. [29] for a detailed discussion of the method. The distance between the two reflection spots was $\Delta x = (400 \pm 3)$ mm, and the distance from the second spot to the screen was x_s , which varied for different channels. The screen was filmed by a CCD camera with a frame rate of 30 Hz. For each measurement, 600 images were taken. The oscillation amplitudes A_1^0 and A_2^0 were determined by a Fourier transformation approach [29]. The calculated Fourier spectrum had a resolution of 0.05 Hz. Every excitation frequency used in the measurements matched a frequency in the discrete spectrum, and we obtained a sharp peak at this very frequency. As the second laser beam covers a smaller distance between the surface and the screen, we have to correct its amplitude to compare it with the oscillation amplitude of the first laser:

$$A_{2,\text{corr}}^0 = A_2^0 \left(1 + \frac{\Delta x}{x_s}\right). \quad (12)$$

Now, the exponential growth rate b of the linear free surface wave is given by [36]

$$b = \frac{\ln(A_{2,\text{corr}}^0/A_1^0)}{\Delta x}. \quad (13)$$

For $b < 0$, the wave amplitude decreases in the streamwise direction and therefore the flow is *stable* against perturbations with frequency f . For $b > 0$, the wave is growing and the flow is *convectively unstable*. The neutral curve is given by $b = 0$.

For our measurements, we have to ensure that the basic flow in the investigated area is fully developed and does not change between the two reflection spots. For this purpose, we measured the surface velocity [30] along the channel and identified the inflow and outflow area where the velocity is not constant. For our experiments, a good choice for x_1 was 600 mm.

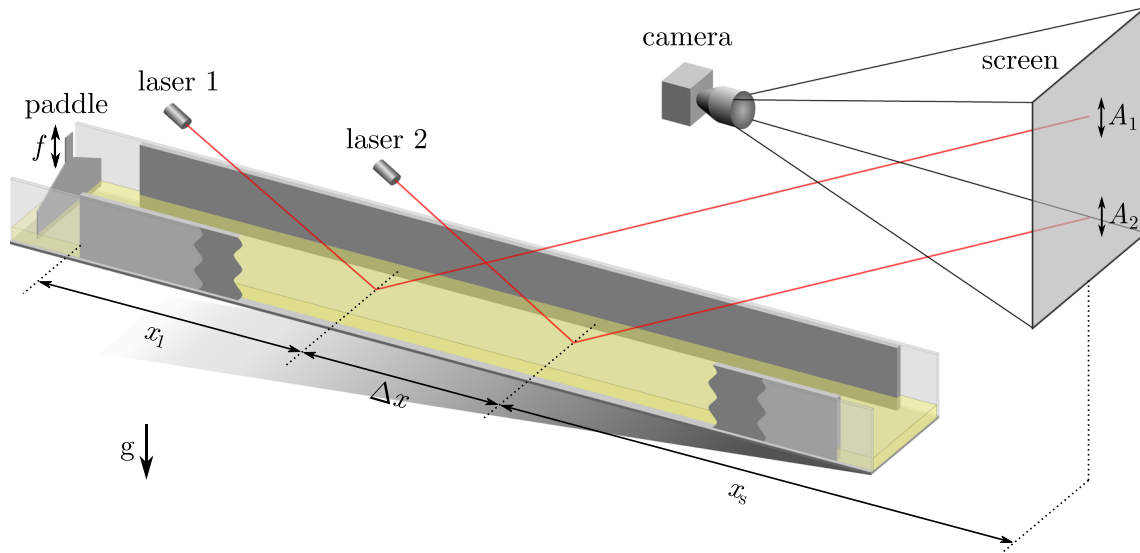


Fig. 3 Setup for measuring the linear instability

4.2 Measurement of the wavelength

The measurement of the wavelength of the free surface waves with frequency f can be done with the same setup as the measurement of the linear stability (Fig. 3). For this purpose, we use the fact that for a sinusoidal wave with frequency f the oscillation of the second laser is proportional to the first, but with a time delay Δt :

$$A_2(t) \propto A_1(t - \Delta t). \quad (14)$$

To calculate the time delay, we extract the phases φ_1 and φ_2 of the signals $A_1(t)$ and $A_2(t)$ (see Eq. 11) from the Fourier spectrum at the excitation frequency f . The *measured phase difference* $\Delta\varphi_0$ is given by

$$\Delta\varphi_0 = (\varphi_1 - \varphi_2) \bmod 2\pi, \quad \Delta\varphi_0 \in [0, 2\pi). \quad (15)$$

Because the phases φ_1 and φ_2 are 2π -periodic, also the measured phase difference $\Delta\varphi_0$ is 2π -periodic. The modulo term is necessary so that $\Delta\varphi_0$ is in the range $[0, 2\pi)$. Since we do not know how many full waves lie between the two measurement positions, we cannot directly achieve the *real phase difference* $\Delta\varphi$, which is generally larger than the measured phase difference:

$$\Delta\varphi = \Delta\varphi_0 + 2\pi n, \quad n \in \mathbb{N}_0, \quad (16)$$

where n is the number of full waves between the measurement positions. In order to obtain n , we performed multiple measurements with increasing frequency f . We expect the experimental data to be similar to the theoretical prediction for the wavelength of the plane flow (see Sect. 3). Therefore, we can assume the wavelength at $f = 1$ Hz to be much larger than the distance between the measurement positions Δx . In this case n equals 0. With increasing frequency, the real phase difference $\Delta\varphi$ must increase since more and more full waves lie within Δx . Figure 4a shows an example of $\Delta\varphi$ and $\Delta\varphi_0$ as well as the theoretical prediction of both as a function of f . When $\Delta\varphi$ exceeds 2π or multiples thereof, we can see a jump down in $\Delta\varphi_0$. In this case we have to increase n for all higher frequencies by one. As one can see, the so obtained values of the real phase difference $\Delta\varphi$ match the theoretical prediction very well.

From the real phase difference, we can now derive the time delay

$$\Delta t = \frac{\Delta\varphi}{2\pi f} = \frac{1}{f} \left(\frac{\Delta\varphi_0}{2\pi} + n \right). \quad (17)$$

From the time delay and the spatial distance between the measurement positions, we can calculate the phase velocity

$$c = \frac{\Delta x}{\Delta t} = \frac{\Delta x f}{\frac{\Delta\varphi_0}{2\pi} + n}, \quad (18)$$

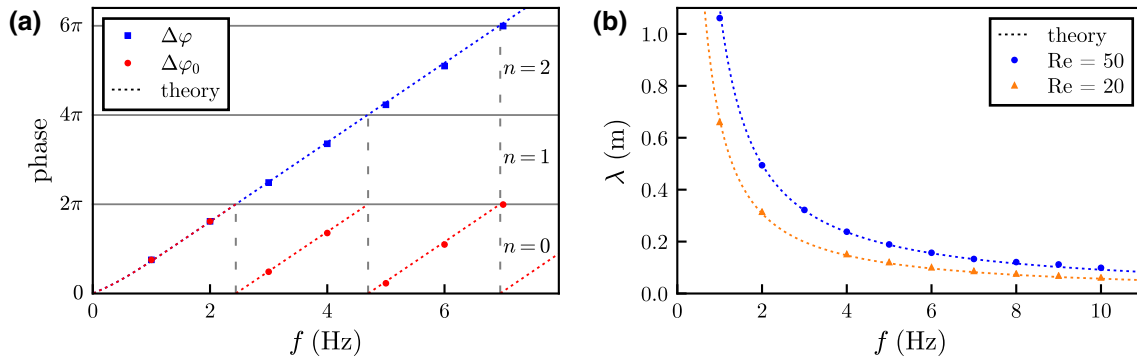


Fig. 4 **a** Real and measured phase difference $\Delta\varphi$ and $\Delta\varphi_0$ as a function of the excitation frequency f with $B = 100$ mm, $\alpha = 10^\circ$ and $\text{Re} = 50$. The dotted lines show the two-dimensional theoretical predictions. **b** Measured and theoretical wavelength for $B = 100$ mm, $\alpha = 10^\circ$ and $\text{Re} = 50$, respectively, $\text{Re} = 20$. The dotted lines show the two-dimensional theoretical predictions

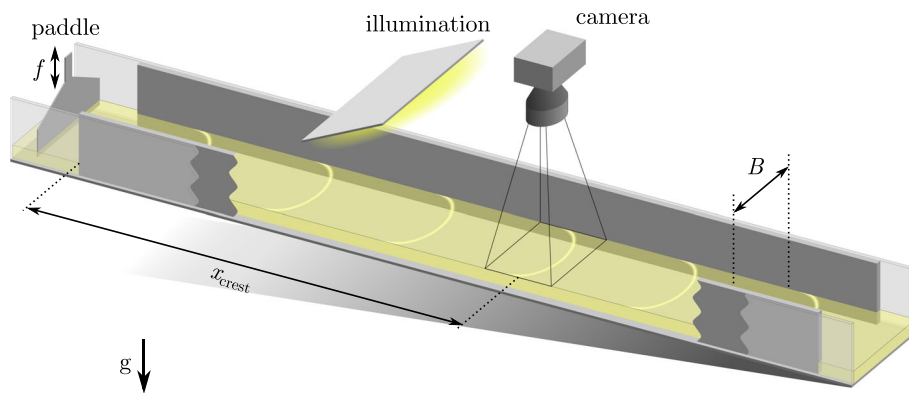


Fig. 5 Setup for measuring the wave's crest line

and finally the wavelength

$$\lambda = \frac{c}{f} = \frac{\Delta x}{\frac{\Delta\varphi_0}{2\pi} + n}. \quad (19)$$

Figure 4b shows an example of the measured and theoretical wavelengths for two different Reynolds numbers. We performed experiments with different channel widths B , inclination angles α and Reynolds numbers Re . All measurements match the two-dimensional theoretical predictions very well, independent of the system parameters. The small derivations of less than 3% are mainly caused by the uncertainty of the Reynolds number Re (see Sect. 2) and the distance Δx (see Sect. 4.1).

4.3 Measurement of the curvature of the crest line

To measure the shape of the crest line, we use the setup shown in Fig. 5. On top of the channel, a camera is mounted. The measurement position $x_{\text{crest}} = 800$ mm is in the center of the measurement position for the linear stability (see Sect. 4.1). Next to the camera, we mounted an areal LED panel that illuminates the fluid surface. The reflection of the light at the part of the surface wave with an appropriate slope is recorded by the camera; see Fig. 6a for an exemplary image. In fact, the recorded bright line is not exactly the crest of the wave, but since we are only interested in the form of the wave and not the exact position of the crest, this difference does not matter. After subtracting a background image, we can extract the crest line—after applying a moving average filter—by searching for the maximum brightness along each vertical pixel column in the image. An example for a detected crest line is given in Fig. 6b. For a reliable measurement, we average 10–30 crest lines, which gives us also an statistic error estimation. After calibrating the result, we obtain the crest line in the form $x_{\text{crest}}(z)$. The spanwise coordinate z origins at the left side of the channel (according to the images taken

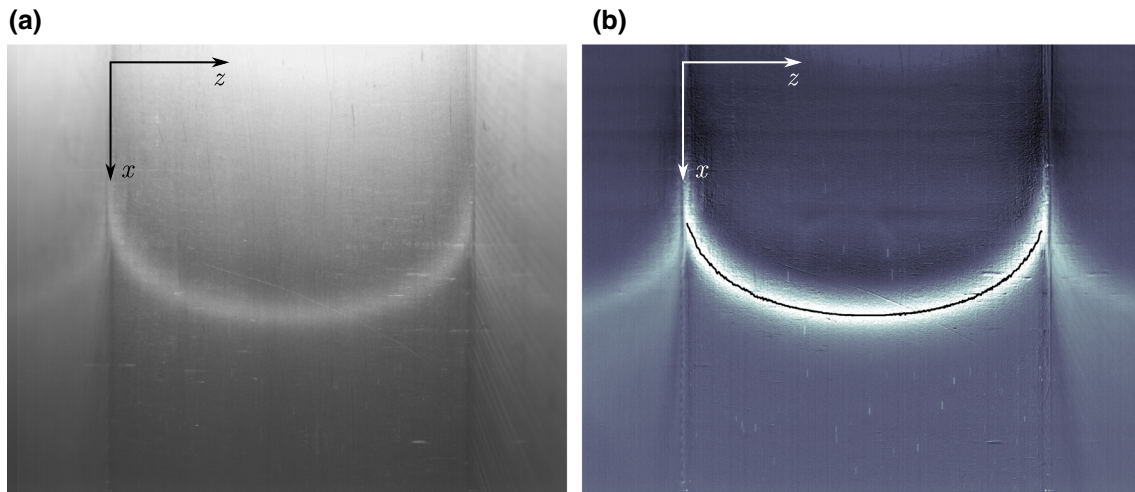


Fig. 6 **a** Original image of a wave crest at $f = 4$ Hz, $B = 129$ mm, $Re = 40$, **b** image subtracted by background, the black line shows the detected crest line. The flow direction is from top to bottom

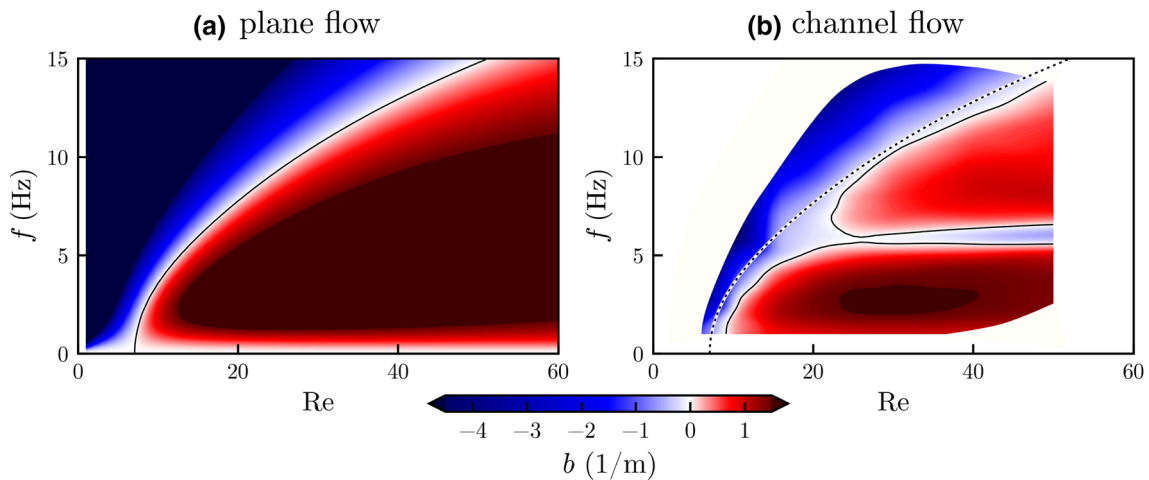


Fig. 7 **a** Theoretical stability chart of the plane flow and **b** measured stability chart of the channel flow for $\alpha = 10^\circ$, $B = 170$ mm and the fluid *Elbesil 140*. The growth rate b is color-coded; the black solid line represents the neutral curve $b = 0$. In the white areas, no measurements were performed. The dotted line in **b** shows the theoretical neutral curve for the plane flow [c.f. (a)] (color figure online)

by the camera, see Fig. 6), whereas the origin of the streamwise coordinate x , which is in general the inflow of the channel, could be chosen arbitrary, since the streamwise position of the wave within the frame has no practical meaning.

We calculate the center curvature k of the crest line via a weighted quadratic fit over the center half of the channel ($\frac{1}{4}B < z < \frac{3}{4}B$):

$$x_{\text{fit}}(z) = -\frac{k}{2} \left(z - \frac{B}{2} \right)^2 + a \left(z - \frac{B}{2} \right) + x_0, \quad (20)$$

where $B/2$ is the center of the channel and k , a and x_0 are the fit parameters. The term $a \approx 0$ is necessary to compensate a small potential asymmetry of the wave, whereas x_0 is the arbitrary streamwise position of the wave.

5 Results and discussion

Figure 7 shows (a) the theoretical stability chart of the plane flow and (b) the measured stability chart of an open channel flow with flat side walls and flat substrate. The channel flow shows an unexpected horizontal stable band in the middle of the unstable area of the plane flow. Until now, the occurrence of fragmented neutral curves and additional unstable isles was only known for undulated substrates, but not for channels without corrugations. We show here that fragmentation occurs not only in “undulated” systems, but also in “flat” systems with side walls. To investigate this new phenomenon, we perform a parameter study to determine the dependency of the stabilization on the system parameters (i.e., excitation frequency, Reynolds number, channel width, inclination angle and viscosity). Finally, we pose the question: Is this stabilization only an effect of flat side walls? Or do we also see this phenomenon in a channel with corrugated side walls?

5.1 Linear instability

The measured stability charts for different inclination angles α and channels widths B are depicted in Fig. 8. In the white areas at the margin of the charts, no measurements were performed. Particularly for low Reynolds numbers or high frequencies, the growth rates were often too small to measure. In subfigure (h) we were not able to reach a higher Reynolds number due to the finite pumping capacity. We could observe a switching [23, 25] between three different patterns of the stability chart when changing the system parameters. At large channel widths (subfigure (h)) there is one single unstable area, similar to the stability chart of the plane flow (dotted line). Decreasing the channel width, the unstable area splits into two separate isles divided by a horizontal stable band (subfigures (g) and (f)). Finally, with further reduction, the high frequency isle disappears since the stable band becomes wider and moves to higher frequencies (subfigures (e) and (d)). This effect is the same for all inclination angles. For $\alpha = 5^\circ$ the system is generally more stable than for $\alpha = 10^\circ$ and therefore there is no unstable isle at high frequencies within our measurement range. On the other hand, for $\alpha = 15^\circ$ the system is generally less stable and therefore the stable band occurs only at smaller channel widths. All stability charts show a local minimum of the growth rate, regardless of whether there is a stable band or not, qualitatively indicated by the yellow line. The frequency of the minimum is nearly the same for all inclination angles but depends strongly on the channel width.

A more detailed visualization of the stabilization is shown in Fig. 9, where the growth rate b is plotted as a function of the excitation frequency f for the Reynolds number $Re = 30$ and several channel widths B . At very low and very high frequencies, the measured growth rate generally approaches the theoretical curve for the plane flow, but at intermediate frequencies a distinct minimum can be seen. The occurrence of a single minimum indicates a stabilizing effect at a certain frequency range. A destabilizing effect, as it may occur in systems with corrugated substrates [20], is not present. The position of the minimum depends strongly on the channel width B . One can also see that the damping is generally stronger for smaller channels.

To ensure that the measured damping is not an artifact of the experimental setup, we performed identical measurements in two channels with different geometric dimensions, pumps and other peripherals (see Sect. 2 and Table 2). Figure 10 shows the growth rate at $Re = 40$ for $\alpha = 10^\circ$, and $B = 170$ mm measured with *Elbesil 140* in channel 1 and channel 2. The two curves show qualitatively almost the same damping phenomenon, and only the position of the minimum is shifted by ≈ 0.5 Hz. Thus, the effect could be verified and we also could achieve an estimation for the measurement accuracy.

The important result of this section is the fact that the frequency at which the minimum of the growth rate occurs shows no significant dependency on the inclination angle. On the other hand, the theoretical neutral curve of the plane flow clearly depends on the inclination angle. Therefore, the damping is an effect that is generally unrelated to the two-dimensional instability. In other words, the damping occurs whether the two-dimensional flow is stable or unstable and the position of the damping band is unrelated to the growth rate of a two-dimensional wave at this frequency. The decisive parameter for the damping is the channel width. Therefore, we can assume the damping as an additional effect caused by the side walls that is independent of the basic instability of the plane flow of infinite extent.

5.2 Frequency and wavelength of maximum damping

In this section, we investigate the dependencies of the damping on the following system parameters: the Reynolds number Re , the channel width B and the inclination angle α . We can assume the damping to be

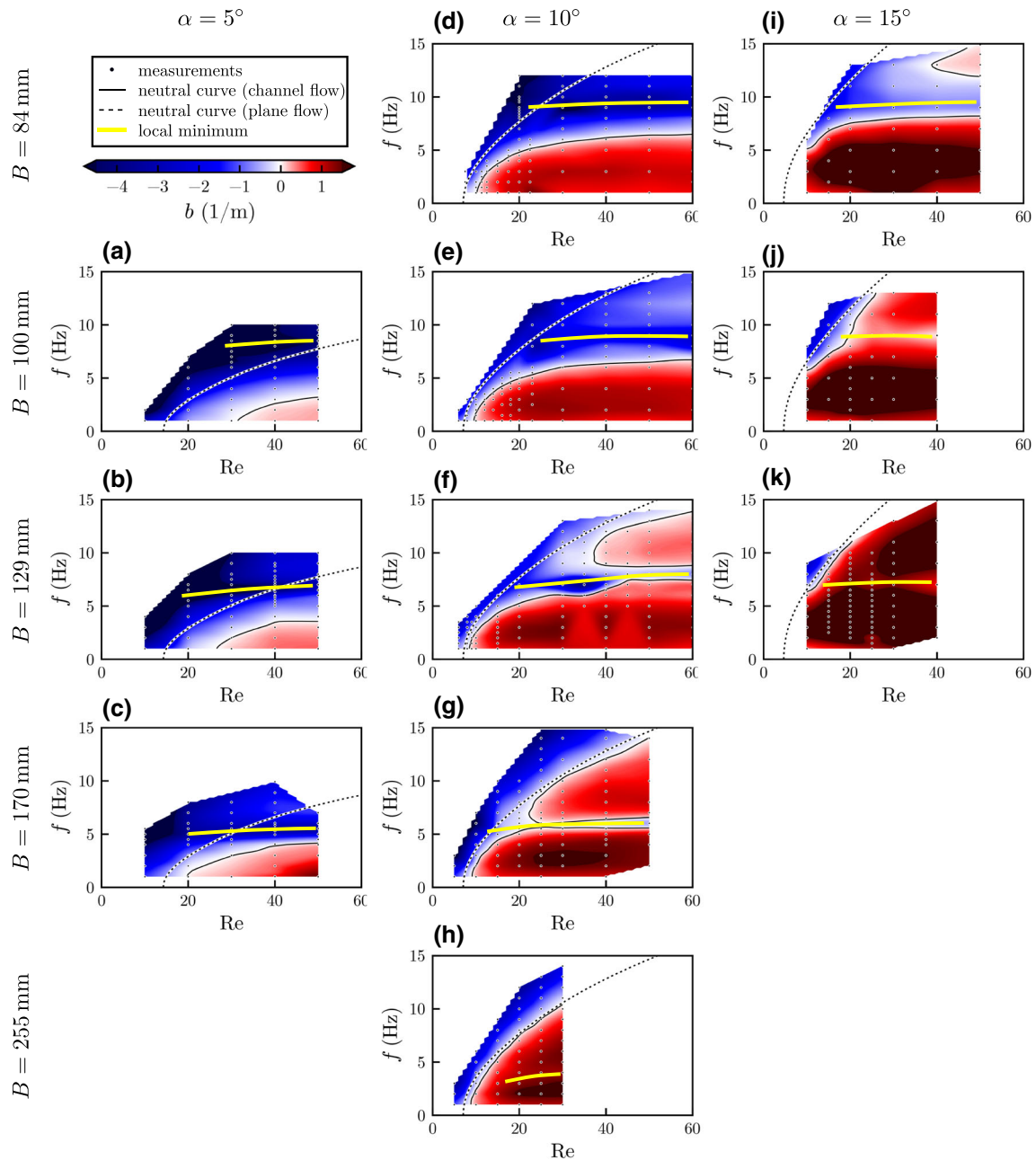


Fig. 8 Stability charts for different inclination angles α and channel widths B measured with the fluid *Elbesil 140*. The individual measurement positions are marked as black dots. The growth rate b is color-coded; stable areas are marked blue, and unstable areas are marked red. In the white areas, no measurements were performed. The black solid lines denote the measured neutral curves, and the black dotted lines the theoretical neutral curves of the plane flow. The yellow solid lines qualitatively show the local minima of the growth rate (color figure online)

an effect that is independent of the instability of the plane flow (see Sect. 5.1). Therefore, we can write the measured growth rate b of the three-dimensional channel flow (here referred as b_{3D}) as the sum of the growth rate of the two-dimensional plane flow b_{2D} and an independent term Δb describing the damping:

$$b_{3D} = b_{2D} + \Delta b. \quad (21)$$

The damping term Δb includes all effects caused by the side walls. Therefore, it must vanish for infinite large channel widths. An example of Δb is given in Fig. 11. To characterize the typical frequency of the damping,

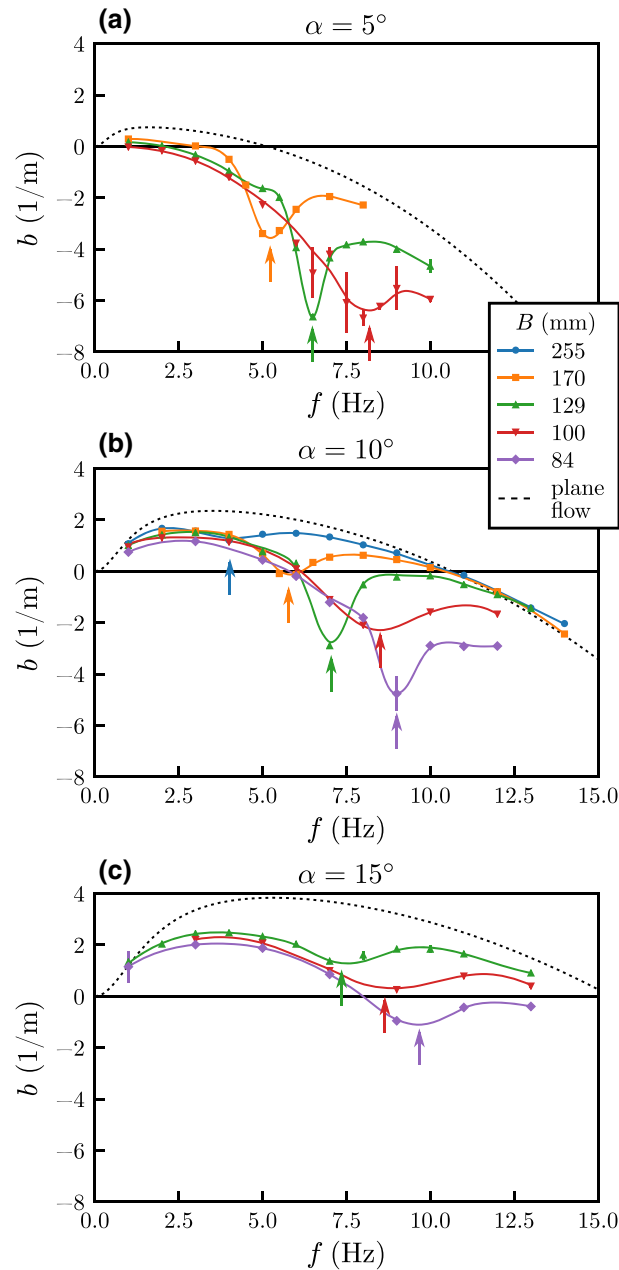


Fig. 9 Growth rate b as a function of the excitation frequency f for $Re = 30$ and different channel widths B . The inclination angle is **a** $\alpha = 5^\circ$, **b** $\alpha = 10^\circ$, **c** $\alpha = 15^\circ$. The arrows highlight the positions of the minima, and the dotted lines show the theoretical growth rate of the plane flow. The measurements were performed with the fluid was *Elbesil 140*

we fit a parabola to the region of the minimum, as shown in Fig. 11. The frequency of the local minimum is referred to as *damping frequency* f_{\min} . We assume an error of 0.5 Hz, based on the reproducibility of the curves (see Fig. 10) and the distance of our measurement points. The corresponding wavelength λ_{\min} , referred to as *damping wavelength*, can be calculated from f_{\min} as discussed in Sect. 4.2. The error of λ_{\min} can be calculated via error propagation, including the error of f_{\min} and Re .

Figure 12 shows f_{\min} and λ_{\min} as a function of the Reynolds number Re . In (a) and (c) one can see that f_{\min} slightly increases with Re . For large Reynolds numbers, f_{\min} barely depends on Re . Since the wavelength is not only a function of the frequency, but also of the Reynolds number, λ_{\min} generally increases with Re , which can be seen in (b) and (d). The dependency on the inclination angle α is also not notable: Figs. 12c, d

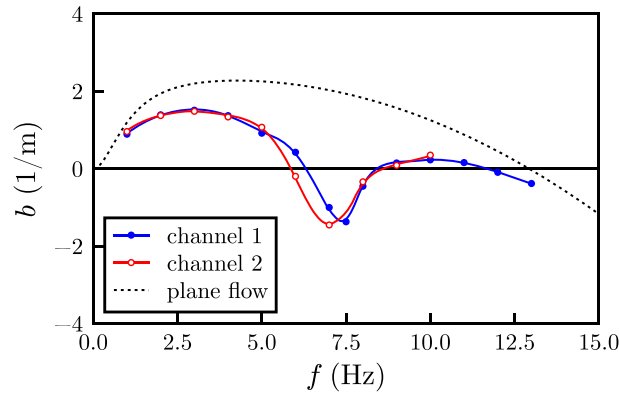


Fig. 10 Verification of the experiment: growth rate b as function of f for $Re = 40$, $\alpha = 10^\circ$, $B = 129$ mm measured in two different channels (see Table 2) with the fluid *Elbesil 140*. The dotted line shows the theoretical growth rate of the plane flow

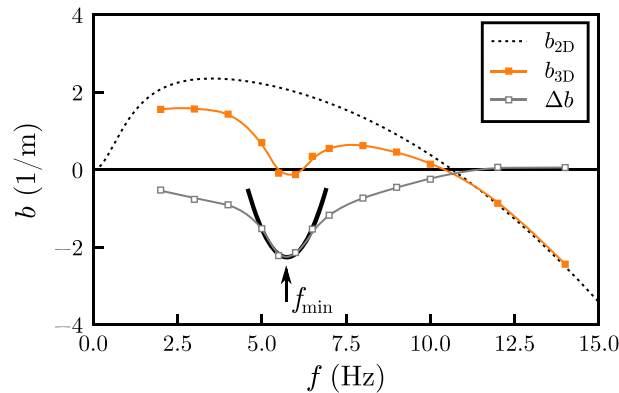


Fig. 11 An example for determining the damping frequency f_{\min} . The orange squares denote the measured growth rate of the channel flow b_{3D} , and the dotted black line the theoretical growth rate for the two-dimensional flow b_{2D} . The damping term $\Delta b = b_{3D} - b_{2D}$ (see Eq. (21)) is shown in gray. The black solid line shows a parabolic fit around the minimum of Δb , indicated by the arrow. The measurement was done at $Re = 30$, $\alpha = 10^\circ$ and $B = 170$ mm with the fluid *Elbesil 140* (color figure online)

show that f_{\min} as well as λ_{\min} barely depend on α . It is not possible for f_{\min} and λ_{\min} both to be independent of α , because the wavelength λ is a function of the frequency f and the inclination angle α . Therefore, if f_{\min} was independent of α , λ_{\min} would have to vary with α . So at least one of the two quantities f_{\min} and λ_{\min} must vary with α . With our data, we cannot determine a clear dependency, but we see that in our measurement range the effect of the inclination angle is rather small compared to the channel width, which will be discussed in the following.

A very strong dependency exists between f_{\min} , respectively λ_{\min} , and the channel width B . One can see in Figs. 12a, b that for increasing channel widths the damping frequency f_{\min} strongly decreases and the damping wavelength λ_{\min} strongly increases. A more detailed plot is shown in Fig. 13, where the dependency of the damping on the channel width is plotted. Figure 13a shows the monotonous decreasing of f_{\min} with increasing B for all inclination angles α . As one can see in Fig. 13b, the damping wavelength λ_{\min} increases monotonously with the channel width B , so for a wider channel longer waves are damped. But since there is no linear dependency, there is no strict matching of the wavelength and the channel width.

Exemplarily, we want to show the influence of another system parameter: the viscosity η . We performed an additional measurement with the fluid *Elbesil 100* (see Sect. 2) in channel number 3 with the channel width $B = 129$ mm at an inclination angle $\alpha = 10^\circ$. Since the pumping power in this setup was limited, we were only able to reach a Reynolds number of 28. Figure 14 shows a comparison of the two measurements with identical parameters, except for the viscosity. One can clearly see that the damping effect occurs for both viscosities. Also the frequency of the damping matches for both measurements.

A more quantitative representation of Fig. 14 is shown in Fig. 15, where the damping frequency f_{\min} is shown for different viscosities. It can be seen that the two lines representing the two viscosities fit together almost perfectly. The damping frequency f_{\min} is not visibly affected by the viscosity. However, since the

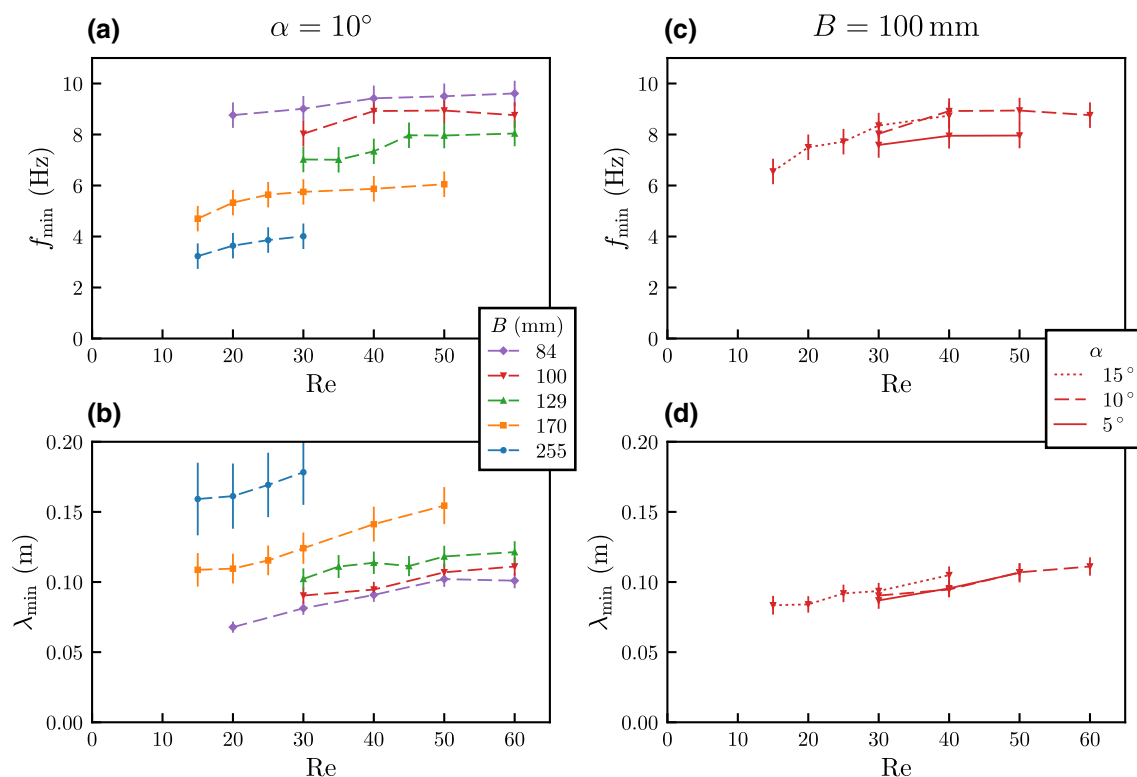


Fig. 12 **a** Damping frequency f_{\min} and **b** damping wavelength λ_{\min} as a function of the Reynolds number Re for a fixed inclination angle $\alpha = 10^\circ$ and different channel widths B . **c** f_{\min} and **d** λ_{\min} as a function of Re for the fixed channel width $B = 100$ mm and different inclination angles α . The fluid was *Elbesil 140*

numerical calculations show that the wavelength of the wave with given frequency and Reynolds number varies when changing the viscosity of the fluid, the damping wavelength λ_{\min} must be affected. In our case there is a shift of approximately 10%. It is not clear how a change in the viscosity causes a change in the damping wavelength, but not in the damping frequency.

To summarize this section, we have shown several dependencies of f_{\min} and λ_{\min} on our system parameters: both quantities barely depend on the inclination angle α but strongly on the channel width B . The Reynolds number Re has a minor effect on f_{\min} , but a significant effect on λ_{\min} . The viscosity has no visible impact on the damping frequency, but on the damping wavelength. We did not find a matching of two quantities and especially no dimensionless number to describe the dependency of the damping on the system parameters. Nevertheless, we were able to find clear and explicit trends in the dependencies.

5.3 Influence of side wall corrugations

We now pose the question: is the newly found damping only an effect of flat side walls? Or can we see this phenomenon also in a corrugated system? And if so, does the side wall corrugation increase this effect? To this end, we performed experiments in a channel with flat substrate and corrugated side walls (see Sect. 2) and varied the streamwise tip distance. The results are depicted in Fig. 16, where the stability chart of a channel flow within flat side walls is compared to those of channels with corrugated side walls. The inclination angle α , the viscosity η and the channel width B are the same for all measurements. For our measurements, we varied the streamwise tip distance L from 5 to 100 mm. Figure 16 clearly shows that the damping is not only an effect of flat walls, but also occurs in channels with corrugated side walls. Qualitatively, the stability charts show the same horizontal stabilization; only the position is significantly shifted to lower frequencies.

A more quantitative representation of Fig. 16 is shown in Fig. 17, where the damping frequency f_{\min} is shown for the different side wall configurations. The corrugated side walls show a very strong effect: as one can see, for all tip distances L the curve is significantly shifted to lower frequencies compared to the case of

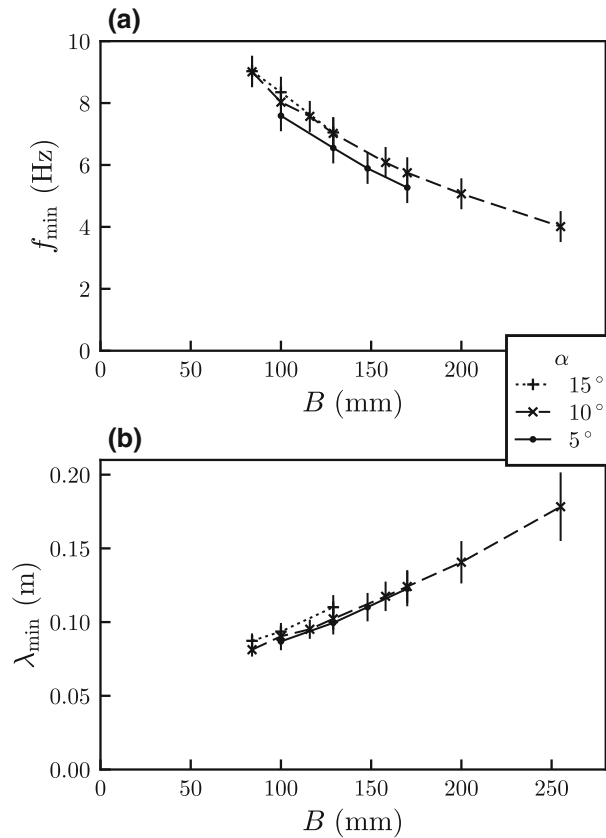


Fig. 13 **a** Damping frequency f_{\min} and **b** damping wavelength λ_{\min} as a function of the channel width B for three different inclination angles α at $Re = 30$. The fluid was *Elbesil 140*

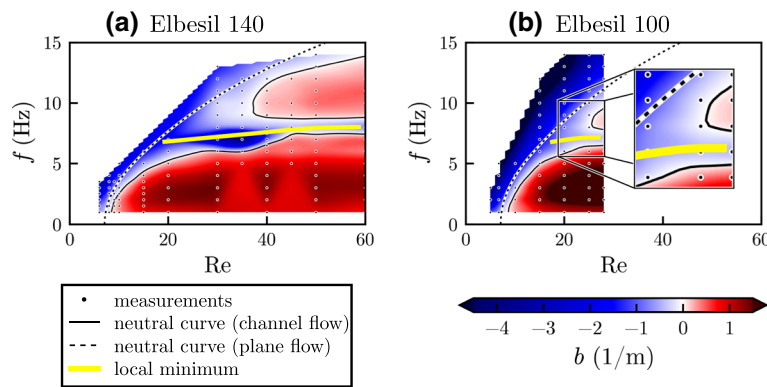


Fig. 14 Stability charts for $\alpha = 10^\circ$, $B = 129$ mm and two different viscosities **a** $\eta = 136.7$ mPa s (*Elbesil 140*) and **b** $\eta = 99.4$ mPa s (*Elbesil 100*). In the white areas, no measurements were performed. The yellow line qualitatively indicates the position of the local minimum of the growth rate. The dotted line shows the theoretical neutral curve for the plane flow of infinite extent (color figure online)

flat side walls. This shift is not a monotonous function of L . The maximum shift occurs for $L = 20$ mm; for smaller and larger tip distances, the shift is less pronounced. This is consistent with the limiting cases of L . For $L \rightarrow 0$, the effect of the corrugation vanishes and the “corrugated” system converges to a “flat” system with channel width B (see Fig. 2). Also for $L \rightarrow \infty$, the system converges to a system with flat side walls, but with the channel width $B + 2l_t$. The difference between the two limiting cases is rather small compared to the maximum shift in f_{\min} for intermediate tip distances.

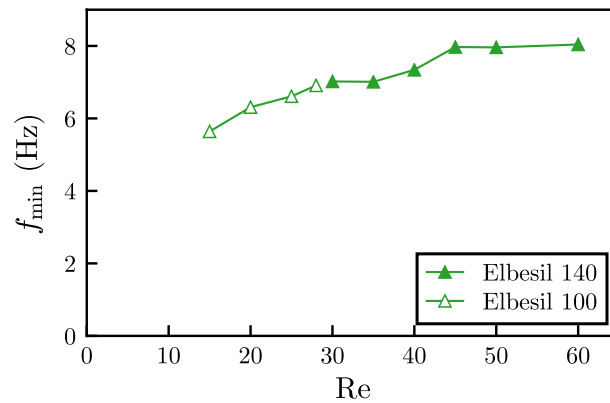


Fig. 15 Damping frequency f_{\min} as a function of the Reynolds number Re for $\alpha = 10^\circ$, $B = 129$ mm and two different viscosities (see Sect. 2)

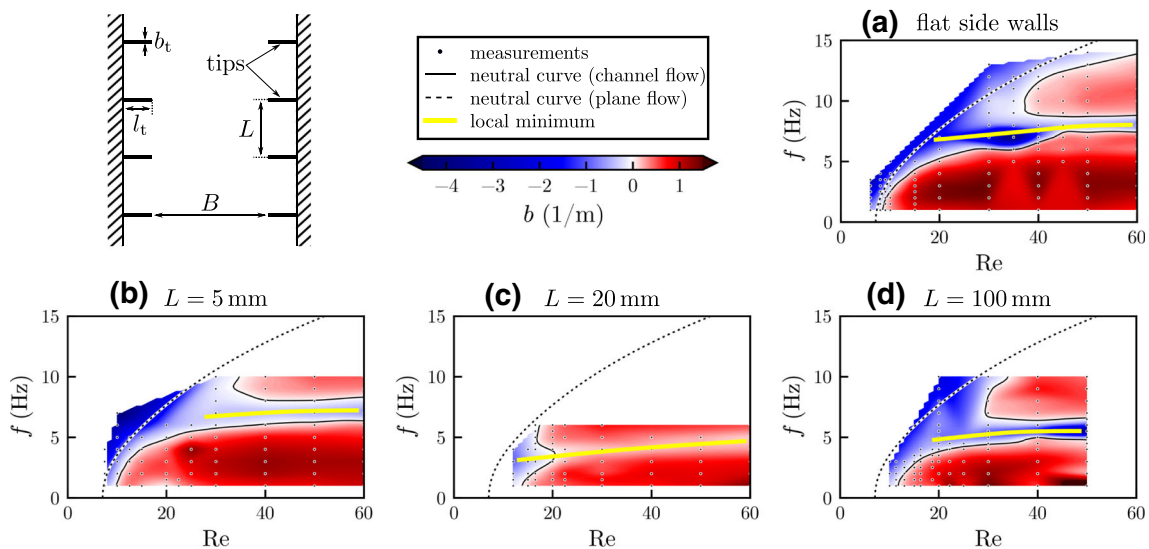


Fig. 16 Stability charts for different side wall configurations: **a** flat side walls, **b–d** corrugated side walls: **b** $L = 5$ mm, **c** $L = 20$ mm, **d** $L = 100$ mm. In the white areas no measurements were performed. The yellow lines qualitatively indicate the position of the local minimum of the growth rate. The dotted lines show the theoretical neutral curves for the plane flow. The measurements were performed with the fluid *Elbesil 140* at $\alpha = 10^\circ$ and $B = 129$ mm (color figure online)

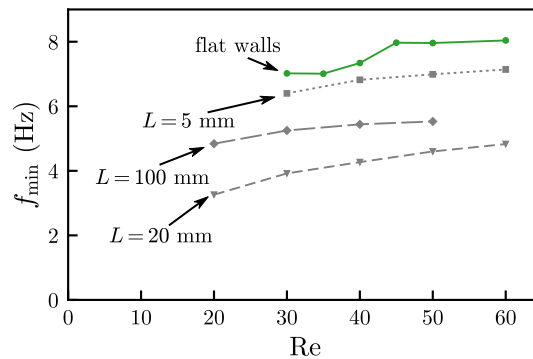


Fig. 17 Damping frequency f_{\min} as a function of the Reynolds number Re . In green the measurement with flat side walls is shown. The gray lines show f_{\min} for corrugated side walls with different tip distances. The measurements were performed with the fluid *Elbesil 140* at $\alpha = 10^\circ$ and $B = 129$ mm (color figure online)

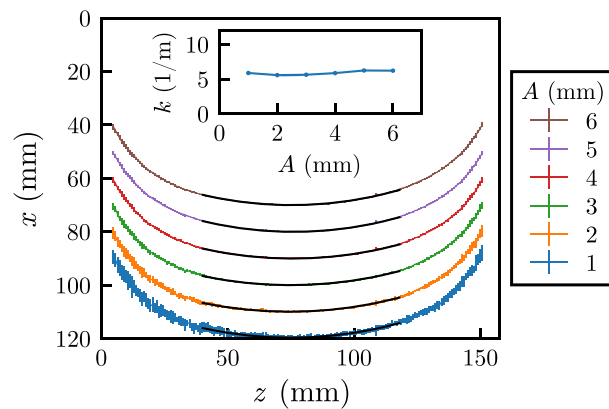


Fig. 18 Averaged crest lines of waves with excitation frequency $f = 9$ Hz and different paddle amplitudes A . The channel width is $B = 158$ mm, denoted by the right border. The different lines are shifted for a better display. The black solid lines show the quadratic fits over the center half of each crest line. The dependency of the curvature k on the paddle amplitude A is shown in the inset. The measurements were performed with the fluid *Elbesil 140* at $\alpha = 10^\circ$, $B = 158$ mm and $Re = 40$

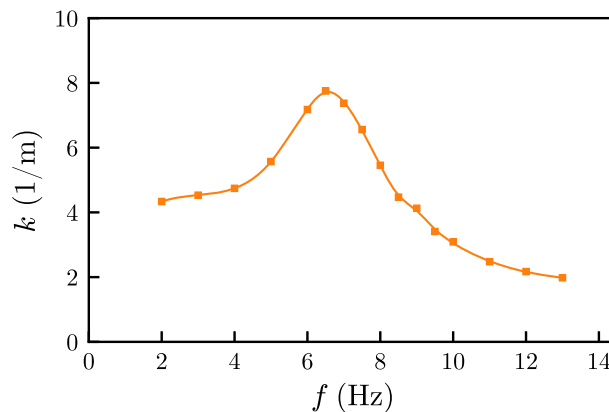


Fig. 19 Curvature k of the crest line depending on the excitation frequency f . The measurements were performed with the fluid *Elbesil 140* at $\alpha = 10^\circ$, $B = 170$ mm and $Re = 30$

A similar phenomenon can be found in the work of Kögel and Aksel [30]. They found that the critical Reynolds number (the neutral curve at $f \rightarrow 0$) is shifted to higher values for corrugated side walls. As in our case, the effect vanishes for the limiting cases $L \rightarrow 0$ and $L \rightarrow \infty$ and has a maximum at intermediate tip distances.

We showed here that the newly found damping is not an effect of flat side walls exclusively, but of side walls in general. Corrugated side walls show qualitatively the same phenomenon, whereas the damping frequency shifts to significantly lower values.

5.4 Connection between the damping and the curvature of the crest line

In the following section, we want to provide a possible attempt at explanation for the selective damping presented in this paper. Since waves in a channel of finite width are not strictly two-dimensional, we are interested in the transverse influence of the side walls. The side walls massively affect the growth rate of the wave, as examined in this paper. On the other hand, it is reported that the side walls also affect the shape of the wave [27, 31]. To be precise, the crest line of a wave in a channel is curved, and this curvature changes with the channel width. So we pose the question: Is there any relation between the damping and the curvature of the crest line?

The curvature k is defined by a quadratic fit (Eq. (20)) over the center half of the wave's crest line (see Sect. 4.3). First of all, we investigate the influence of the wave's amplitude on the crest line curvature. For the measurement of the curvature k , we need large amplitudes and therefore nonlinear waves. On the other hand,

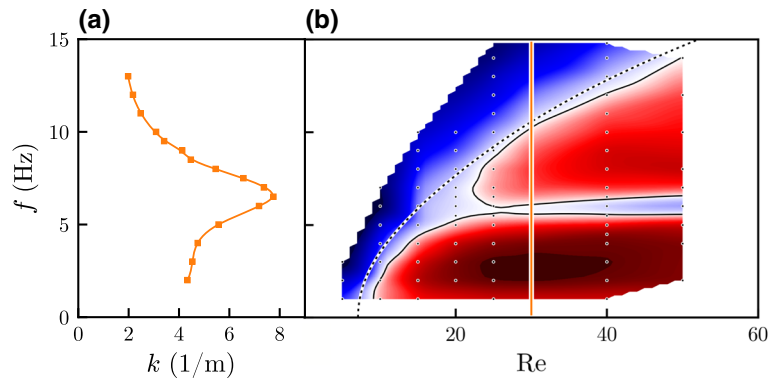


Fig. 20 **a** Curvature k of the crest line for $Re = 30$, $B = 170$ mm and $\alpha = 10^\circ$ (see Fig. 19). **b** Corresponding stability chart (see Fig. 3). The orange solid line in **b** marks $Re = 30$ (color figure online)

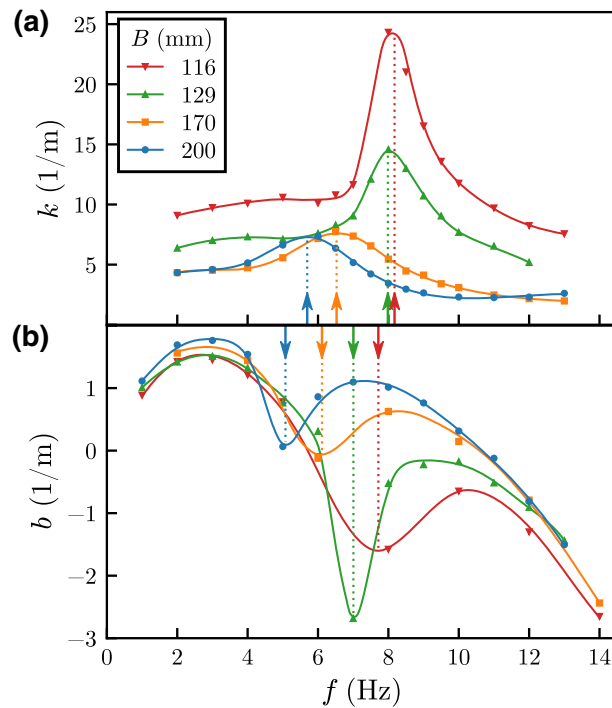


Fig. 21 **a** Curvature k of the crest line and **b** growth rate b as a function of the excitation frequency f for different channel widths B at $Re = 30$, $B = 170$ mm and $\alpha = 10^\circ$. The fluid was *Elbesil 140*. The arrows highlight the frequency of the maximum curvature, respectively the frequency of the minimum growth rate

for the measurement of the stability small amplitudes and therefore linear waves are necessary. Thus, we want to know if the wave's amplitude has any impact on the curvature k . In fact, the curvature of the crest line is independent of the amplitude, as demonstrated in Fig. 18. We performed several measurements with different paddle amplitudes A , which result in different wave amplitudes at the measurement position. As one can see, the curvature k , displayed in the inlay of Fig. 18, is constant for all amplitudes. The experiment was repeated with different frequencies between 3 and 9 Hz, and all results show that the curvature k is independent of the amplitude. Therefore, we can assume the same curvature for linear waves.

Figure 19 shows an example of the curvature k depending on the excitation frequency f . We see the astonishing result that k is not a monotonous function of f , but shows a maximum at around 6.5 Hz. Very long and very short waves have a smaller curvature than waves of intermediate length. The decreasing of k at high frequencies is consistent with the findings of Leontidis et al. [31]. As far as we know, a maximum in the curvature was not yet reported.

The occurrence of an unexpected maximum in the curvature k at a certain frequency is interesting, especially because the corresponding stability chart shows an unexpected damping at a similar frequency (see Fig. 20). Therefore, we now compare the curvature of the crest line and the growth rate of the waves. Figure 21 shows (a) the growth rate b and (b) the curvature k as a function of f for several channel widths B . The channel width has two significant effects on the curvature: first, the curvature generally increases for smaller channels, which is consistent with prior works [27,31]. Second, the frequency of the maximum curvature decreases with the channel width, similar to the minimum of the growth rate. The arrows in Figs. 21a, b indicate the positions of the maxima respectively the minima. As one can see, these positions are at similar frequencies and show the same trend; only the maximum of the curvature is at slightly higher frequencies than the minimum of the growth rate. We see that there is a correlation between the curvature of a wave's crest line and the wave's growth rate. A similar correlation can be found in the work of Vlachogiannis et al. [27], who showed that reducing the channel width leads to an increase in both the curvature of the crest line and the critical Reynolds number.

On the basis of our observations, we speculate that there is a relationship between the curvature k and the growth rate b of a wave in a channel flow. The exact interaction between a wave's shape and the instability of its underlying basic flow as well as the physical background of both phenomena requires further investigations.

6 Conclusions

In this work, we studied the effect of side walls on the stability of open channel flows with flat substrate and flat side walls against free surface perturbations. To this end, we carried out multiple experiments with different system parameters (the Reynolds number, the excitation frequency, the inclination angle, the channel width and the viscosity) and measured the growth rate and the wavelength of the waves as well as the curvature of its crest line. We have shown that—in comparison with the two-dimensional flow of infinite extent—side walls have a dramatic influence on the stability of the flow and the shape of the neutral curve. We have also shown that this is not only an effect of flat side walls, but also of corrugated side walls. Finally, we found a connection between the growth rate of the wave and the curvature of the wave's crest line.

The stability chart of the open channel flow shows, if the system parameters are suitable, an additional unstable isle separated by a horizontal stable band. Until now, such a fragmentation of the neutral curve was only known for systems with undulated substrates [21–25]. We could observe a switching [23,25] between three different patterns of the stability chart (see Fig. 8). At large channel widths or large inclination angles, there is one single unstable area. Decreasing the channel width or the inclination angle, the unstable area splits in two disjunct isles. Finally, with further reduction, the high frequency isle disappears. By investigating the growth rate, we found that the fragmentation of the neutral curve was caused by a selective damping of waves within a certain frequency range. These waves were characterized by the frequency and wavelength of the maximum damping. We found that the damping frequency barely depends on the inclination angle. On the other hand, the instability of the two-dimensional flow strongly depends on the inclination angle. Since a change in the inclination angle leads to a change in the two-dimensional instability but not in the damping frequency, we can assume that the damping and the two-dimensional instability are generally unrelated. Therefore, the damping caused by the side walls is an additional effect to the underlying two-dimensional instability.

Within our measurement range, the damping frequency shows no strong dependency on the inclination angle, the Reynolds number or the viscosity. The decisive parameter is the channel width. The wider the channel, the smaller is the damping frequency. On the other hand, we see a dependency of the damping wavelength on the Reynolds number and the viscosity, but not on the inclination angle, at least for our measurement range. However, also for the damping wavelength the decisive parameter is the channel width: the wavelength increases with the channel width. Although we did not find a matching of two quantities and especially no dimensionless number to describe the dependency of the damping on the system parameters, we were able to find clear and explicit trends in the dependencies.

We showed that a fragmentation of the neutral curve is not only an effect of corrugated substrates, but also of side walls. So what if these side walls are corrugated? We found that the qualitative structure of the stability chart is the same for flat as well as for corrugated side walls. Only the damping frequency is shifted significantly to lower values, depending on the streamwise length scale of the corrugations. For the limiting cases of very large and very small corrugation lengths, the shift vanishes. This is consistent with the fact that in these limits the “corrugated” system converges to a “flat” system. However, the exact interaction between side walls, especially corrugated side walls, and waves is highly complex and requires further investigations.

Side walls do not only have an effect on the growth rate of a wave, but also on its shape. We found that the center curvature of the crest line dramatically depends on the excitation frequency and the channel width. The influence of the channel width on the curvature has been studied by Leontidis et al. [31] for a small frequency range, which we were able to confirm. However, the frequency has a much more interesting effect on the curvature of the crest line, which has not been observed until now: for a fixed channel width, the curvature shows a distinct maximum at a certain frequency. Very short and very long waves have a smaller curvature than intermediate waves. The position of the maximum strongly depends on the channel width. For smaller channels the maximum shifts to higher frequencies. This shift correlates with a high degree to the shift of the damping frequency when varying the channel width. We therefore speculate that there is a relationship between the crest line curvature and the growth rate (respectively decay rate) of surface waves in a channel flow. These results open up new directions in the research on the stability of film flows. The exact interaction between a wave's shape and the instability of its underlying basic flow as well as the physical background of both phenomena requires further investigations.

Acknowledgements The authors acknowledge Marion Märkl and Stephan Eißner for their help in carrying out the experiments.

References

1. Kistler, S.F., Schweizer, P.M.: Liquid Film Coating. Springer, Dodrecht (1997). <https://doi.org/10.1007/978-94-011-5342-3>. ISBN: 978-94-010-6246-6
2. Weinstein, S.J., Ruschak, K.J.: Coating flows. *Ann. Rev. Fluid Mech.* **36**(1), 29–53 (2004). <https://doi.org/10.1146/annurev.fluid.36.050802.122049>
3. Gugler, G., Beer, R., Mauron, M.: Operative limits of curtain coating due to edges. *Chem. Eng. Process. Process Intensif.* **50**(5), 462–465 (2011). <https://doi.org/10.1016/j.cep.2011.01.010>
4. Webb, R.L.: Principles of Enhanced Heat Transfer. Wiley, New York (1994)
5. Vlasogiannis, P., Karagiannis, G., Argyropoulos, P., Bontozoglou, V.: Air-water two-phase flow and heat transfer in a plate heat exchanger. *Int. J. Multiph. Flow.* **28**(5), 757–772 (2002). [https://doi.org/10.1016/S0301-9322\(02\)00010-1](https://doi.org/10.1016/S0301-9322(02)00010-1)
6. Greve, R., Blatter, H.: Dynamics of Ice Sheets and Glaciers. Springer, Berlin (2009). <https://doi.org/10.1007/978-3-642-03415-2>
7. Luca, I., Hutter, K., Tai, Y.C., Kuo, C.Y.: A hierarchy of avalanche models on arbitrary topography. *Acta Mech.* **205**(1), 121–149 (2009). <https://doi.org/10.1007/s00707-009-0165-4>
8. Hutter, K., Svendsen, B., Rickenmann, D.: Debris flow modeling: a review. *Contin. Mech. Thermodyn.* **8**(1), 1–35 (1994). <https://doi.org/10.1007/BF01175749>
9. Kumar, A., Karig, D., Acharya, R., Neethirajan, S., Mukherjee, P.P., Retterer, S., Doktycz, M.J.: Microscale confinement features can affect biofilm formation. *Microfluid. Nanofluidics* **14**(5), 895–902 (2013). <https://doi.org/10.1007/s10404-012-1120-6>
10. Braun, R.J.: Dynamics of the tear film. *Ann. Rev. Fluid Mech.* **44**, 267–297 (2012)
11. Nusselt, W.: Die Oberflächenkondensation des Wasserdampfes. *VDI Z* **60**, 541–546 (1916)
12. Scholle, M., Aksel, N.: An exact solution of visco-capillary flow in an inclined channel. *Z. Angew. Math. Phys.* **52**(5), 749–769 (2001). <https://doi.org/10.1007/PL00001572>
13. Haas, A., Pollak, T., Aksel, N.: Side wall effects in thin gravity-driven film flow—steady and draining flow. *Phys. Fluids* **23**(6), 062107 (2011). <https://doi.org/10.1063/1.3604002>
14. Kapitza, P.L.: Wavy flow of thin layers of viscous liquid. *Zh. Eksper. Teoret. Fiz.* **18**, 3–28 (1948)
15. Kapitza, P.L., Kapitza, S.P.: Wavy flow of thin layers of a viscous fluid. *Zh. Eksp. Teor. Fiz.* **19**, 105–120 (1949)
16. Benjamin, T.B.: Wave formation in laminar flow down an inclined plane. *J. Fluid Mech.* **2**(06), 554 (1957). <https://doi.org/10.1017/S00222112057000373>
17. Yih, C.-S.: Stability of liquid flow down an inclined plane. *Phys. Fluids* **6**(3), 321 (1963). <https://doi.org/10.1063/1.1706737>
18. Vlachogiannis, M., Bontozoglou, V.: Experiments on laminar film flow along a periodic wall. *J. Fluid Mech.* **457**, 133–156 (2002). <https://doi.org/10.1017/S00222112001007637>
19. Wierschem, A., Aksel, N.: Instability of a liquid film flowing down an inclined wavy plane. *Phys. D Nonlinear Phenomena* **186**(3), 221–237 (2003). [https://doi.org/10.1016/S0167-2789\(03\)00242-2](https://doi.org/10.1016/S0167-2789(03)00242-2)
20. D'Alessio, S.J.D., Pascal, J.P., Jasmine, H.A.: Instability in gravity-driven flow over uneven surfaces. *Phys. Fluids* **21**(6), 062105 (2009). <https://doi.org/10.1063/1.3155521>
21. Heining, C., Aksel, N.: Effects of inertia and surface tension on a power-law fluid flowing down a wavy incline. *Int. J. Multiph. Flow* **36**(11), 847–857 (2010). <https://doi.org/10.1016/j.ijmultiphaseflow.2010.07.002>
22. Pollak, T., Aksel, N.: Crucial flow stabilization and multiple instability branches of gravity-driven films over topography. *Phys. Fluids* **25**(2), 024103 (2013). <https://doi.org/10.1063/1.4790434>
23. Schörner, M., Reck, D., Aksel, N., Trifonov, Y.: Switching between different types of stability isles in films over topographies. *Acta Mech.* **229**(2), 423–436 (2018). <https://doi.org/10.1007/s00707-017-1979-0>
24. Schörner, M., Reck, D., Aksel, N.: Does the topography's specific shape matter in general for the stability of film flows? *Phys. Fluids* **27**(4), 042103 (2015). <https://doi.org/10.1063/1.4917026>
25. Schörner, M., Aksel, N.: The stability cycle—a universal pathway for the stability of films over topography. *Phys. Fluids* **30**(1), 012105 (2018). <https://doi.org/10.1063/1.5003449>

26. Aksel, N., Schörner, M.: Films over topography: from creeping flow to linear stability, theory, and experiments, a review. *Acta Mech.* **229**(4), 1453–1482 (2018). <https://doi.org/10.1007/s00707-018-2146-y>
27. Vlachogiannis, M., Samandas, A., Leontidis, V., Bontozoglou, V.: Effect of channel width on the primary instability of inclined film flow. *Phys. Fluids* **22**(1), 012106 (2010). <https://doi.org/10.1063/1.3294884>
28. Georgantaki, A., Vatteville, J., Vlachogiannis, M., Bontozoglou, V.: Measurements of liquid film flow as a function of fluid properties and channel width: evidence for surface-tension-induced long-range transverse coherence. *Phys. Rev. E* **84**(2), 026325 (2011)
29. Pollak, T., Haas, A., Aksel, N.: Side wall effects on the instability of thin gravity-driven films—from long-wave to short-wave instability. *Phys. Fluids* **23**(9), 094110 (2011). <https://doi.org/10.1063/1.3634042>
30. Kögel, A., Aksel, N.: Massive stabilization of gravity-driven film flows with corrugated side walls. *Phys. Fluids* **30**(11), 114105 (2018). <https://doi.org/10.1063/1.5055931>
31. Leontidis, V., Vatteville, J., Vlachogiannis, M., Andritsos, N., Bontozoglou, V.: Nominally two-dimensional waves in inclined film flow in channels of finite width. *Phys. Fluids* **22**(11), 112106 (2010). <https://doi.org/10.1063/1.3484250>
32. Scholle, M., Haas, A., Aksel, N., Wilson, M.C.T., Thompson, H.M., Gaskell, P.H.: Competing geometric and inertial effects on local flow structure in thick gravity-driven fluid films. *Phys. Fluids* **20**(12), 123101 (2008). <https://doi.org/10.1063/1.3041150>
33. Chang, H., Demekhin, E.A.: *Complex Wave Dynamics on Thin Films*, vol. 14. Elsevier, Amsterdam (2002). ISBN 0-08-052953-4
34. Liu, J., Paul, J.D., Gollub, J.P.: Measurements of the primary instabilities of film flows. *J. Fluid Mech.* **250**, 69–101 (1993). <https://doi.org/10.1017/S0022112093001387>
35. Wierschem, A., Lepski, C., Aksel, N.: Effect of long undulated bottoms on thin gravity-driven films. *Acta Mech.* **179**(1), 41–66 (2005). <https://doi.org/10.1007/s00707-005-0242-2>
36. Schörner, M., Reck, D., Aksel, N.: Stability phenomena far beyond the Nusselt flow—revealed by experimental asymptotics. *Phys. Fluids* **28**(2), 022102 (2016). <https://doi.org/10.1063/1.4941000>
37. Dauth, M., Schörner, M., Aksel, N.: What makes the free surface waves over topographies convex or concave? A study with Fourier analysis and particle tracking. *Phys. Fluids* **29**(9), 092108 (2017). <https://doi.org/10.1063/1.5003574>

Publisher's Note Springer Nature remains neutral with regard to jurisdictional claims in published maps and institutional affiliations.

Terms and Conditions

Springer Nature journal content, brought to you courtesy of Springer Nature Customer Service Center GmbH (“Springer Nature”).

Springer Nature supports a reasonable amount of sharing of research papers by authors, subscribers and authorised users (“Users”), for small-scale personal, non-commercial use provided that all copyright, trade and service marks and other proprietary notices are maintained. By accessing, sharing, receiving or otherwise using the Springer Nature journal content you agree to these terms of use (“Terms”). For these purposes, Springer Nature considers academic use (by researchers and students) to be non-commercial.

These Terms are supplementary and will apply in addition to any applicable website terms and conditions, a relevant site licence or a personal subscription. These Terms will prevail over any conflict or ambiguity with regards to the relevant terms, a site licence or a personal subscription (to the extent of the conflict or ambiguity only). For Creative Commons-licensed articles, the terms of the Creative Commons license used will apply.

We collect and use personal data to provide access to the Springer Nature journal content. We may also use these personal data internally within ResearchGate and Springer Nature and as agreed share it, in an anonymised way, for purposes of tracking, analysis and reporting. We will not otherwise disclose your personal data outside the ResearchGate or the Springer Nature group of companies unless we have your permission as detailed in the Privacy Policy.

While Users may use the Springer Nature journal content for small scale, personal non-commercial use, it is important to note that Users may not:

1. use such content for the purpose of providing other users with access on a regular or large scale basis or as a means to circumvent access control;
2. use such content where to do so would be considered a criminal or statutory offence in any jurisdiction, or gives rise to civil liability, or is otherwise unlawful;
3. falsely or misleadingly imply or suggest endorsement, approval, sponsorship, or association unless explicitly agreed to by Springer Nature in writing;
4. use bots or other automated methods to access the content or redirect messages
5. override any security feature or exclusionary protocol; or
6. share the content in order to create substitute for Springer Nature products or services or a systematic database of Springer Nature journal content.

In line with the restriction against commercial use, Springer Nature does not permit the creation of a product or service that creates revenue, royalties, rent or income from our content or its inclusion as part of a paid for service or for other commercial gain. Springer Nature journal content cannot be used for inter-library loans and librarians may not upload Springer Nature journal content on a large scale into their, or any other, institutional repository.

These terms of use are reviewed regularly and may be amended at any time. Springer Nature is not obligated to publish any information or content on this website and may remove it or features or functionality at our sole discretion, at any time with or without notice. Springer Nature may revoke this licence to you at any time and remove access to any copies of the Springer Nature journal content which have been saved.

To the fullest extent permitted by law, Springer Nature makes no warranties, representations or guarantees to Users, either express or implied with respect to the Springer nature journal content and all parties disclaim and waive any implied warranties or warranties imposed by law, including merchantability or fitness for any particular purpose.

Please note that these rights do not automatically extend to content, data or other material published by Springer Nature that may be licensed from third parties.

If you would like to use or distribute our Springer Nature journal content to a wider audience or on a regular basis or in any other manner not expressly permitted by these Terms, please contact Springer Nature at

onlineservice@springernature.com